AERODYNAMIC DATA BASE GENERATION FOR A RE-USABLE LAUNCHER CONFIGURATION

Jan Vos, Alain Gehri, Giacomo Benedetti

CFS Engineering
EPFL Innovation Park, Bâtiment A
1015 Lausanne, Switzerland

Ansgar Marwege

DLR Institute of Aerodynamics and Flow Technology
Supersonic and Hypersonic Technologies Department
Linder Höhe, 51147 Cologne, Germany

ABSTRACT

In the frame of the ESA funded FLPP project CFD4SALTO Navier Stokes CFD simulations are made for the Themis T3 launcher configuration to generate high-fidelity aerodynamic data bases that will be used to develop the control laws and flight dynamics system. The CFD simulations are made using the Navier Stokes Multi Block solver NSMB. The chimera method was used for the deflection of the grid fins, and the sliding mesh approach was used to avoid that grid points in the boundary layer propagate into the far field. Depending on the Mach number the number of grid points was between 28 and 40 Million.
Calculations were made for both the Ascent configuration (with folded grid fins) and the Descent configuration. The calculation matrix included a large number of points on the ascent and descent trajectory, ranging from low subsonic up to supersonic Mach numbers. Calculations were made without active engines, as well as using 3 active engines for the Ascent configuration, and either 1 or 2 active engines for the Descent configuration (depending on the Mach number and trajectory point).
This paper gives an overview of the different launcher configurations considered, the grid generation strategy, the physical modeling used, and the post processing of the results.

***Index Terms*—** Reusable launchers, Computational Fluid Dynamics, Aerodynamic Data Base Generation.

1. INTRODUCTION

The success of Space-X with the Falcon 9 has shown that it is possible to re-use the first stage of the launcher, thereby significantly reducing the launch costs. Through different projects Europe is also investing in developing technologies for re-usable launch vehicles. Germany, France and Japan work together on a reusable Vertical Take Off Vertical Landing first stage demonstrator in the CALLISTO project (2018-2025) [1]. The EU funded H2020 project RETALT (2019-2022) [2] studied critical technologies in detail, among them Aerodynamics, Aerothermodynamics, Flight Dynamics and Guidance Navigation and Control (GNC), Structures, Mechanisms, Thrust Vector Control and Thermal Protection Systems.
The European Space Agency through its Future Launchers Programme (FLPP) is funding the development of the Themis rocket demonstrator for recovery and reuse of technologies. The Themis vehicle is powered by the reusable Prometheus engine using methane as fuel. In collaboration with the EU funded Horizon Europe project SALTO (2023 - 2026) a series of so-called low altitude Hop tests will be carried out in 2025 for the Themis T1H (Themis 1-Engine Hop) at the Esrange Space Center in Kiruna, Sweden, in order to test critical technologies.
In parallel work has started to design the Themis T3 (3-engine variant) which will cover the full flight domain. This design work is carried out in the SALTO project, with support through the ESA FLPP project CFD4SALTO. The main activities of the CFD4SALTO project are wind tunnel test data processing at DLR in Köln, and CFD simulations performed by CFS Engineering [3].

This paper is concerned with these CFD simulations. The different configurations studied will be discussed, as well as the simulation strategy. Some interesting results are discussed in detail.

2. CONFIGURATIONS

Different launcher configurations are being studied in the CFD4SALTO project, see Fig. 1 for the descent configurations. The ascent configuration has a nose cap. All configurations have in common that details on the launch vehicle as protrusions and ducts are modeled. As a result the configuration is not symmetric. The launcher configuration on the left is the starting point (Aeroshape 1.1). Then from left to right are respectively the configurations with a longer launcher length, a shorter interface, new landing legs and finally with new grid fins (hardly visible in the picture). Aeroshape 1.1 is about 34 meters high, and has a diameter of 3.5 meters.

All configurations have 3 engines. Either 0, 1 or 3 engines are activated in the ascent phase, while in the descent phase

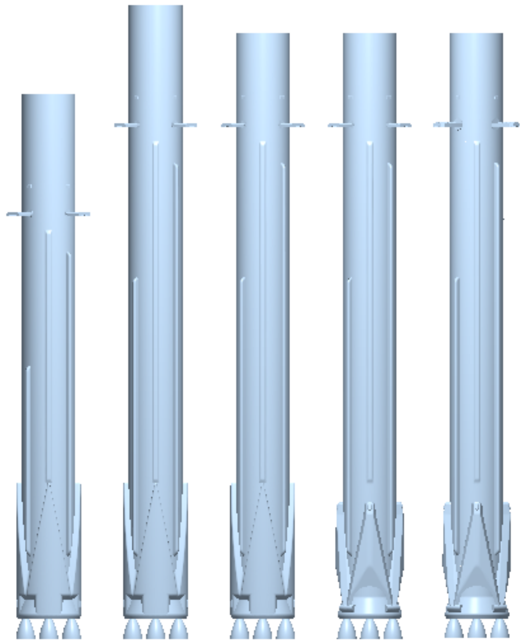

Fig. 1. Descent launcher configurations studied in the CFD4SALTO project.

either 0, 1 or 2 engines are being used.

3. GRID GENERATION

Ansys ICEM CFD was used to generate multiblock structured grids for each configuration. Due to the presence of the nose cap and the folded grid fins different grids are used for the ascent and descent configurations. Also different grids are used for the subsonic and supersonic calculations. Due to the presence of the bow shock in the supersonic calculations it is possible to move the free-stream boundary closer to the body, thereby reducing the number of grid points. The calculation matrix included high altitude supersonic Mach number points, and for these calculations the grid in the boundary layer could have less grid points while still having an y^+ value of the first cell around 1.
The chimera method was used for the grid around the grid fins. In this way simple python scripts can be used to rotate the grid fin without the need to go back to the mesh generator. The sliding mesh strategy was used to avoid that fine grids around the vehicle propagate to the farfield. The first grid cell spacing and the growth rate in the boundary layer followed closely the grid generation rules used for AIAA drag prediction and high-lift prediction workshops.
Figure 2 shows several images of the grid. Depending on the configuration, the phase (ascent or descent) and the Mach number the grid size varied between 28 and 40 Million grid points for the full configuration. The grid was made such that it is possible to obtain a coarse grid by removing every 2nd grid point in each direction. The number of blocks was around 2200 for the ascent configuration and around 14000 for the descent configuration due to the large number of blocks needed to mesh the grid fins.
Each component of the configuration (grid fins, protrusions, nozzles, etc) has it's own boundary condition code to permit the extraction of the aerodynamic forces for each individual component.

(a) Mesh through the grid fins

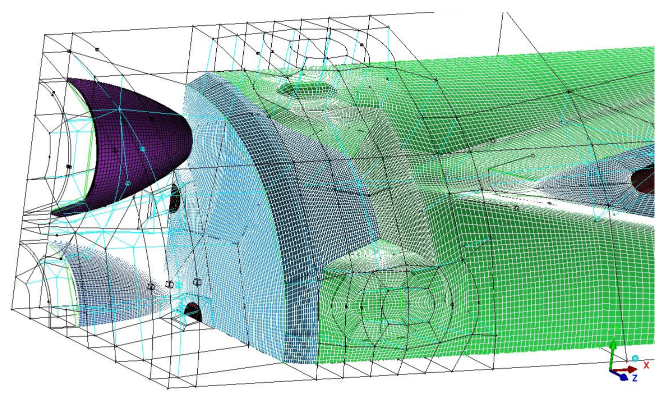

(b) Topology of the base region grid

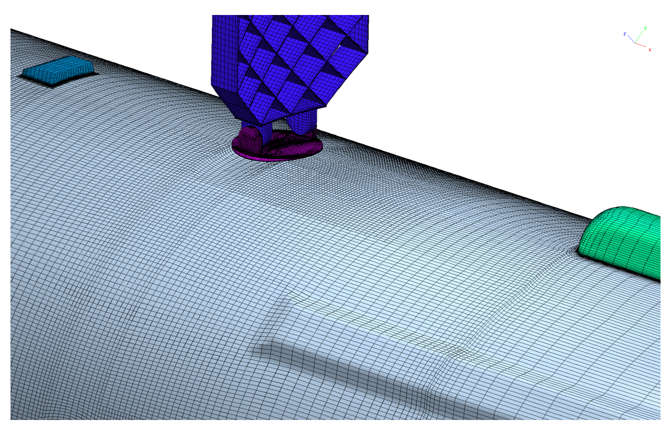

(c) Grid near the attachment of the grid fin

Fig. 2. Views of the grid of the launcher configuration.

4. PHYSICAL AND NUMERICAL MODELING

4.1. CFD Solver

All CFD calculations in the CFD4SALTO project were made using the Navier Stokes Multi Block solver NSMB which is developed in a consortium composed of different universities and industries [4]. NSMB is a cell-centered finite volume solver using multi block structured grids. The patch grid and chimera method are available to simplify the mesh generation for complex geometries, as shown in the previous section. NSMB was also extensively used in the RETALT EU funded project [5, 6].

NSMB includes a large variety of turbulence models and numerical schemes, as well different levels of chemistry modeling.

4.2. Physical modeling

Turbulence was modeled using the one-equation Spalart-Allmaras turbulence model [7]. Calculations without engines were made using the caloric perfect gas assumption. The calculations with active engines assumed a frozen flow for the combustion products. The properties at the nozzle exit (pressure, temperature density and velocity components) were given as function of the radius, and imposed as boundary conditions, see for example Fig. 3.

The chemical composition at the nozzle exit was composed of the species CO2, CO, H, H2, H2O O and O2. The thermal perfect gas assumption was used for a mixture of 8 species (the 7 species from the nozzle exit together with N2). The mixing of the combustion gases from the engines with the free-stream flow was computed using a conserved scalar equation. The local thermodynamic properties were computed using the NASA 9 polynomials [8], and the laminar transport coefficients were calculated using the method available in the Chemkin Package [9]. This permits to calculate the single species viscosity, and Wilke's semi-empirical formula [10] is then used to calculate the laminar mixture viscosity. The species thermal conductivity can be calculated from the species laminar viscosity and the specific heat using the Eucken relation [10] and again Wilke's rule is used to calculate the mixture thermal conductivity.

4.3. Numerical modeling

All calculations were made using the central space discretization scheme with artificial dissipation [11]. A TVD type switch is used to improve the shock capturing properties of the scheme.
The discretized equations are integrated in time using the semi-implicit LU-SGS scheme [12]. The CFL number is increased with a factor 1.005 every time step starting from 0.1 to 10^{12} for the calculations without engine, and to 10^3 for the calculations with active engines. For the calculations with

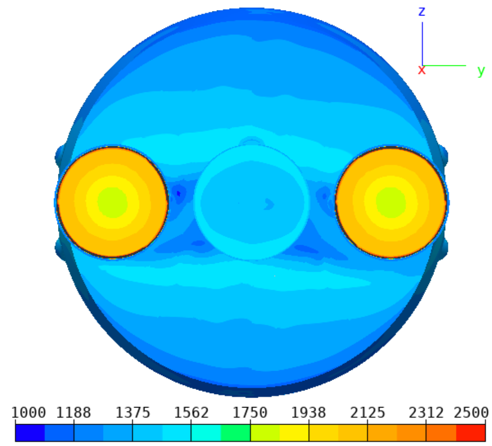

Fig. 3. Temperature at the nozzle exit for the calculations with active engines.

active engine the first 500 steps were made without increasing the CFL number.

5. CALCULATION MATRIX AND STRATEGY

5.1. Ascent Configuration

The calculation matrix for the ascent configuration considered 11 Mach numbers between 0.3 and 3.5 and 5 Angles of Attack, resulting in 55 calculations with no active, 1 active and 3 active engines (in total 165 calculations).

5.2. Descent Configuration

The initial calculation matrix for the descent configuration without active engines considered 11 Mach numbers between 0.3 and 1.5, 6 angles of attack, 8 roll angles and 3 grid fin deflection angles $0^o, \pm 20^o$ for a single grid fin, resulting in 1386 calculations.
With 1 active engine 11 Mach numbers between 0.3 and 3.5 were computed for the same angles of attack, roll angles and grid fin deflections. With 2 active engines only 8 Mach numbers between 0.6 and 3.5 were considered using the same angles of attack and roll angles. For these calculations the grid fins were not deflected. In a later phase the number of calculations was reduced by considering less Mach numbers and fewer angles of attack. In total around 950 calculations were made for Aeroshape 1.1 with active engines.
For the generation of the aerodynamic data bases for the different configurations shown in Fig. 1 only the roll angle of 0^o was used, and the grid fin deflections were set to $[0^o, 0^o, 0^o, 0^o]$, $[20^o, 20^o, -20^o, -20^o]$ and $[-20^o, -20^o, 20^o, 20^o]$ to permit the study of the pitch control. An additional calculation was made for the angle of attack of 180^o with the

grid fin deflections set at $[20^o, 20^o, 20^o, 20^o]$ to study the roll control, resulting in 390 calculations for each configuration.

5.3. Calculation Strategy

First a coarse grid calculation was made (using the same numerical parameters as for the fine grid), running 2000 steps. This solution was then interpolated on the fine grid. Then the fine grid calculation was made running 6000 steps for the subsonic and transonic Mach numbers and 3000 steps for the supersonic Mach numbers. Convergence was judged by looking at the variation of the C_D during the last 1000 or 2000 steps. If this variation was larger than 2% (subsonic and transonic Mach numbers) or 1% (supersonic Mach numbers) additional steps were made. Larger variations in C_D were accepted when the C_D was close to zero, or when after 15000 steps the C_D convergence criterium was not met.

Scripts were written to generate the necessary input files, to launch the jobs and to extract the results.

6. POSTPROCESSING

The aerodynamic data base (AEDB) is delivered as an Excel sheet having as rows the different calculations made, and as columns meta data that permit to identify the calculation (Configuration, Mach number, altitude, grid fin deflections, etc), followed by the aerodynamic coefficients (overall and for each grid fin), followed by information on the engine. In summary the results of each calculation is translated in a row with 54 numbers.

In addition to the information in the AEDB, data repository files were prepared that include tecplot files of different cutplanes as well as detailed information on the aerodynamic forces of the different components.

7. RESULTS

It is impossible to give a detailed discussion on all results obtained. For this reason only some selected results are shown to illustrate flow features.

7.1. Ascent Configuration

Figures 4 and 5 show the Mach number contours in the plane $y = 0$ for a subsonic and supersonic Mach number, using no, 1 and 3 engines. The calculations with engines show the typical structure of Mach disks, indicating regions with lower and higher Mach numbers due to expansion fans and compression waves generated by the interaction of the flow from the nozzles with the surrounding flow. This is in particular visible in Fig. 4.

The supersonic Mach number case is at high altitude, and the expansion of the plumes can be clearly seen for the cases with active engines. The figure also shows the bow shock wave just in front of the nose, as well as shock waves generated by the folded grid fins. It can also be observed that the boundary layer is thicker for the case with 3 active engines.

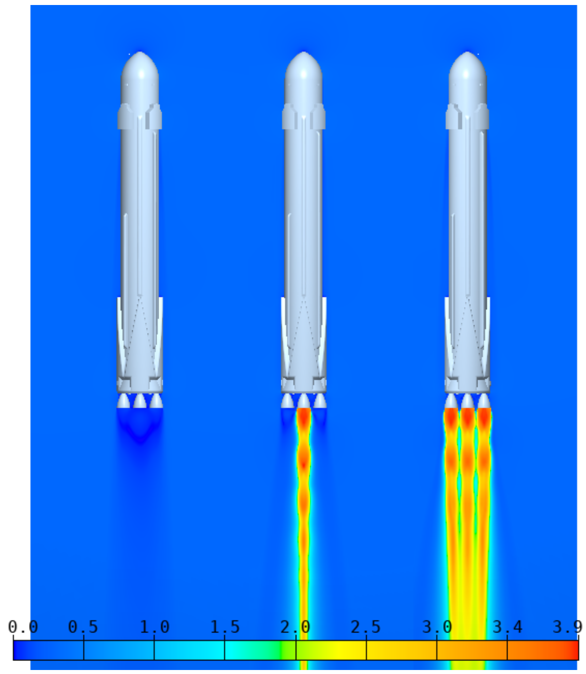

Fig. 4. Mach number contours ascent configuration at $M_\infty = 0.30$.

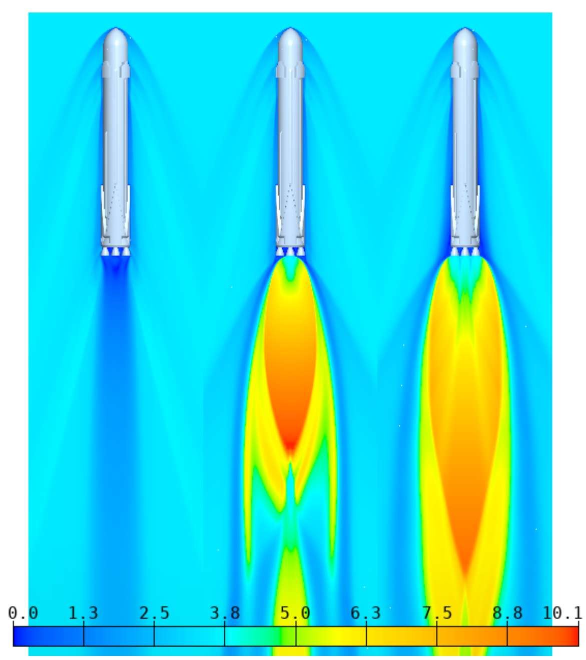

Fig. 5. Mach number contours ascent configuration at $M_\infty = 3.50$.

7.2. Descent Configuration

Figure 6 shows the Mach number contours in the $y = 0$ plane for the calculation at $M_\infty = 0.60$. As for the ascent configuration the Mach disks are clearly visible in the plume when the engines are active. One can observe that the plumes are pushed sideways for the case with 2 engines. It should be mentioned that in this case the flow exhibits some unsteadiness, which is responsible for the asymmetry in the plumes. With active engines there is a subtle balance between the free stream flow (coming from the bottom in the figure), and the plume from the engines.

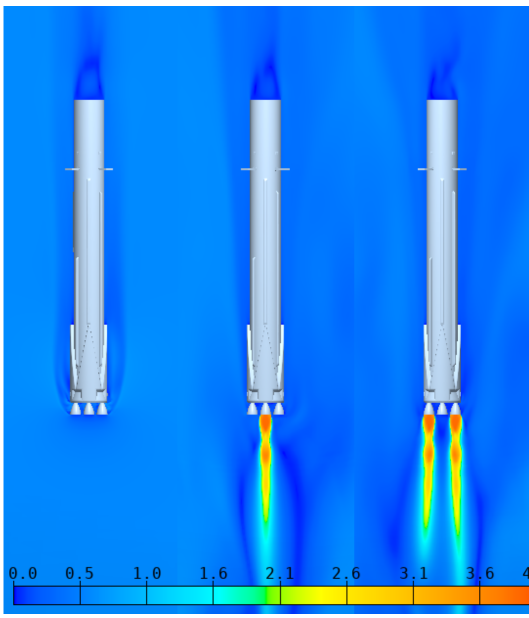

Fig. 6. Mach number contours descent configuration for $M_\infty = 0.60$.

This is further illustrated in Fig. 7. One can clearly see the singular points where the free stream velocity has the exact opposite value of the flow coming from the engines. This leads to the deviation of the free stream flow around the plume, generating several vortical structures. This flow behavior is unsteady, and in general the calculations with active engines are more difficult to converge.

Figure 8 shows the Mach contours in the $y = 0$ plane for different angles of attack for the calculation using 2 engines at $M_\infty = 0.90$. For $\alpha = 180^o$ the plume of the 2 engines are separated, which is less the case for the 2 other angles of attack. For the lowest 2 angles of attack the figure also shows different shock structures in the flow.

It should be mentioned that the calculations for these 2 angles of attack show large separated flow regions, as illustrated in Fig. 9 which shows the Mach number contours and stream lines in the $z = 0$ plane for the case with an $\alpha = 155^o$.

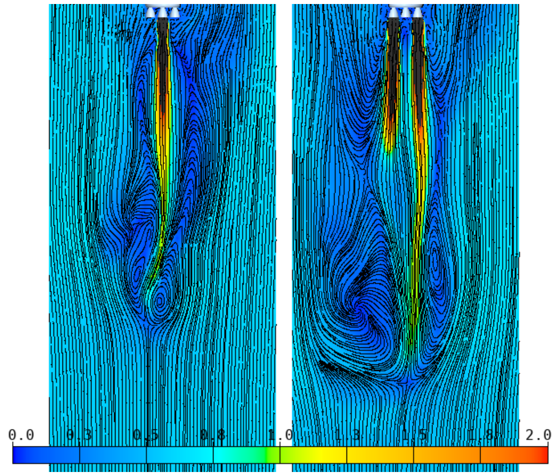

Fig. 7. Mach number contours descent configuration for $M_\infty = 0.60$, zoom of the plume region.

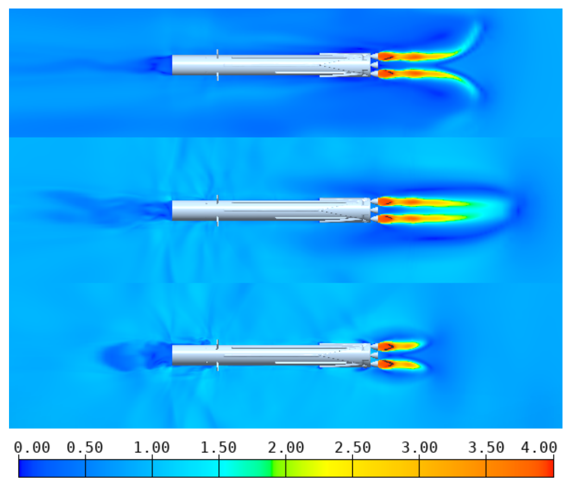

Fig. 8. Mach number contours in the $y = 0$ plane, descent configuration with 2 engines, $M_\infty = 0.90$, top $\alpha = 180^o$, middle $\alpha = 170^o$ and bottom $\alpha = 155^o$.

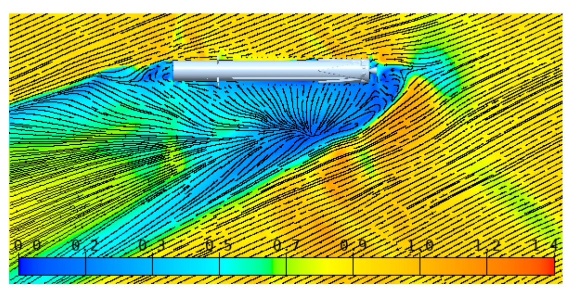

Fig. 9. Mach number contours and stream lines in the $z = 0$ plane, descent configuration with 2 engines, $M_\infty = 0.90$, $\alpha = 155^o$.

Figure 10 shows the Mach number contours in the $y = 0$ plane for the calculation at $M_\infty = 1.20$. One can clearly see the bow shock in the calculation without active engines, as well as different waves generated near the landing legs, grid fins and on top. In the case of active engines the bow shock is pushed away from the nozzle exit. This also leads to larger zones of low velocity around the launch vehicle, as shown in the middle and right figure.

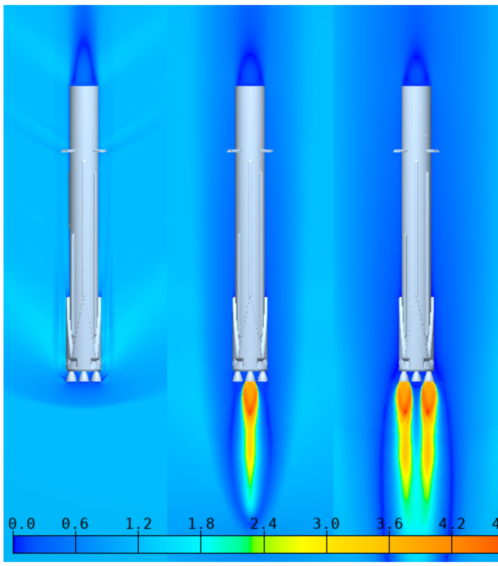

Fig. 10. Mach number contours descent configuration for $M_\infty = 1.20$, $\alpha = 180^o$.

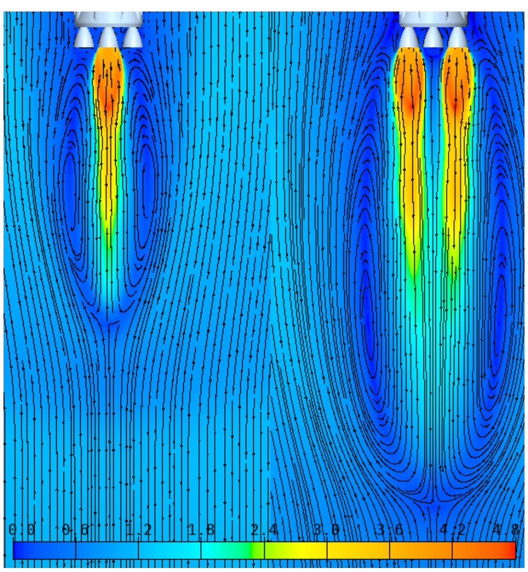

Fig. 11. Mach number contours descent configuration for $M_\infty = 1.20$, $\alpha = 180^o$, zoom of the plume region.

The interaction between the plume from the engines and the supersonic free-stream flow is much more stable than for the subsonic case, see also Fig. 11. One can clearly observe the singular points, and the recirculation regions near the plumes.

Figure 12 shows the velocity contours in a x-cutplane through the landing legs for the calculations with 0 and 2 engines for the descent configuration at $M_\infty = 1.20$. One can clearly observe the small recirculations generated by the 4 landing legs and the 2 ducts. One can also observe that the low velocity region is much larger for the case with 2 engines, meaning that the plumes from the engines push the flow away from the body.

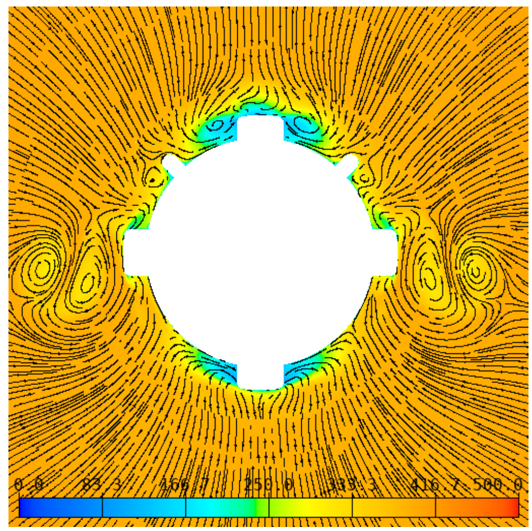

(a) No active engine

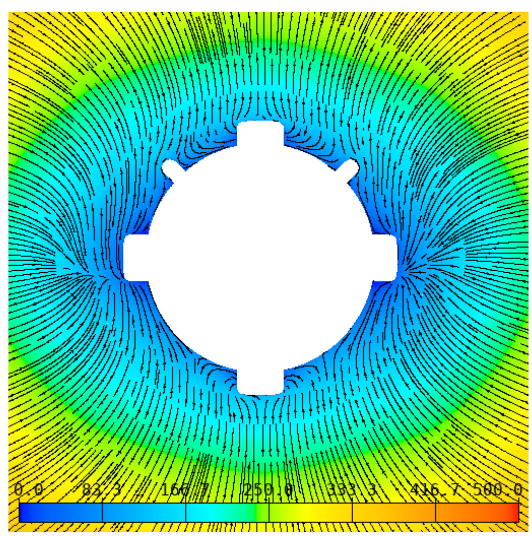

(b) 2 active engines

Fig. 12. Velocity in a x-cut plane near the landing legs, $M_\infty = 1.20$, $\alpha = 180^o$.

The Mach number contours in the $y = 0$ plane for the configuration with 2 engines as function of the free stream Mach number is shown in Fig. 13 Depending on the free stream Mach number the plumes are separated or pushed apart, and might show unsteady behavior. This possible unsteady behavior also affects the aerodynamic coefficients (and the convergence of the calculation).

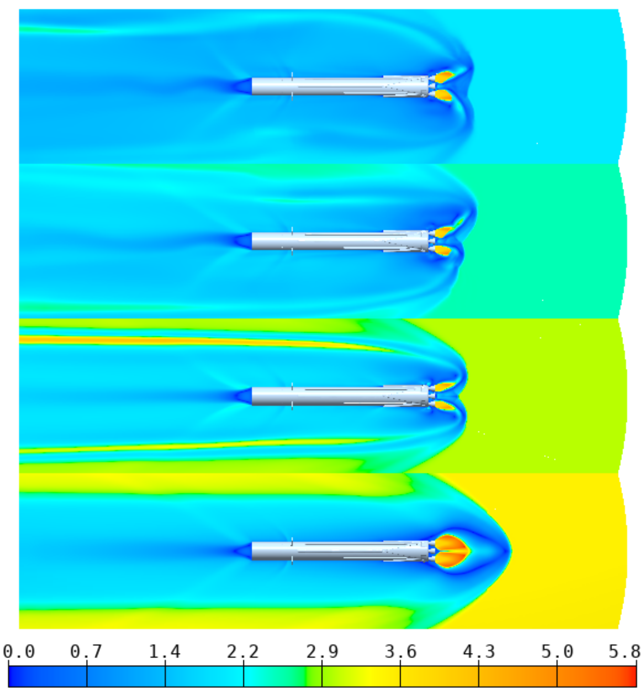

Fig. 13. Mach number contour's descent configuration with 2 engines, from top to bottom: $M_\infty = 2.00$, $M_\infty = 2.50$, $M_\infty = 3.00$, $M_\infty = 3.50$

The computed CX at $M_\infty = 3.00$ for different roll angles phi and angles of attack is shown in Fig. 14. The behavior of the curves are different for the different roll angles. For the roll angles of 0^o and 180^o the CX almost continuously decrease when going from high to lower angle of attack. For these roll angles the two plumes are separated, but stable. For the other roll angles the plumes are asymmetric, and the position and size vary considerably with the angle of attack due to flow separations near the nozzles and the launcher body. Looking at the other Mach numbers (not shown here) showed that for $M_\infty = 3.50$ and $M_\infty = 1.50$ the CX decreases when going from high to low angle of attack for all roll angles phi. For the Mach numbers 3.00, 2.50 and 2.00 for some values of the roll angle the CX increased first with decreasing value of the angle of attack, before decreasing at either $\alpha = 165^o$ or $\alpha = 170^o$.

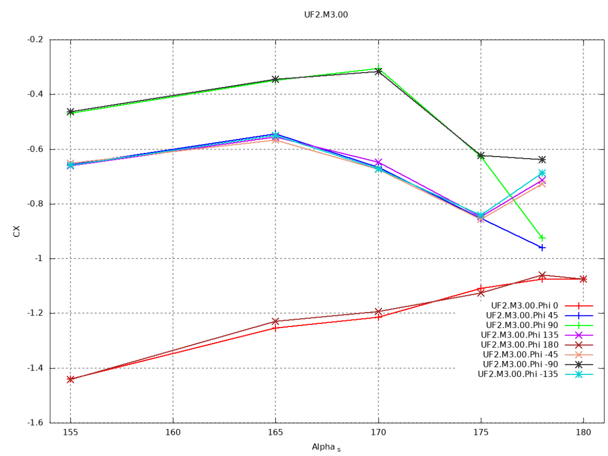

Fig. 14. Computed CX for different roll angles ϕ and angles of attack, $M_\infty = 3.00$

7.3. Configuration with New Landing Legs

Figure 15 shows the velocity contours in the same x-cut plane as Fig. 12 for the configuration with the new landing legs for the calculation without active engines. Comparing this figure with Fig. 12a shows that the new landing legs are more rounded, but have larger zones of low velocity near the launcher body.

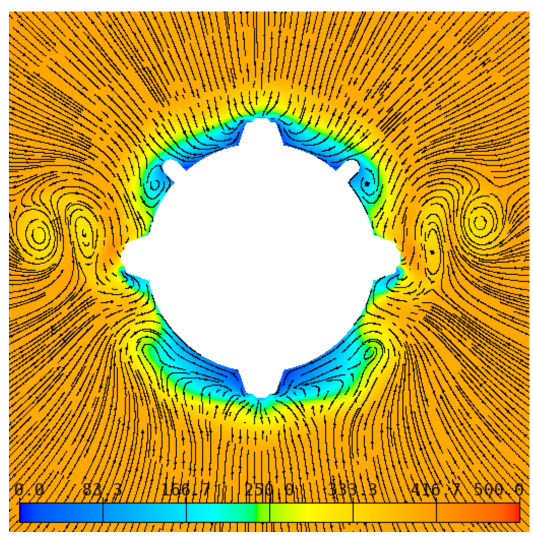

Fig. 15. Velocity in a x-cut plane near the landing legs, $M_\infty = 1.20$, $\alpha = 180^o$, configuration with new landing legs.

7.4. Configuration with New Grid fins

The last configuration from Fig. 1 is the one with new grid fins. In the SALTO project a detailed design study was made of the grid fins for the T3 vehicle [13]. This resulted in a new grid fin which is taller, has rounded leading edges, less, but larger cells. The wall thickness was also increased to comply manufacturing constraints. The new grid fin design gives significant aerodynamic improvements in the transonic flight regime, and some small improvements in the supersonic regime.

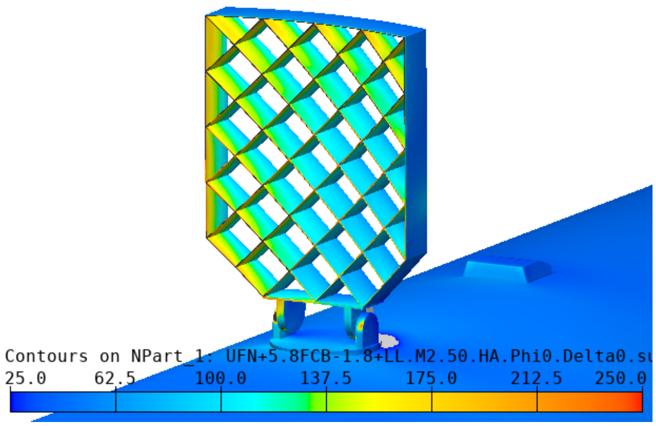

(a) old grid fin

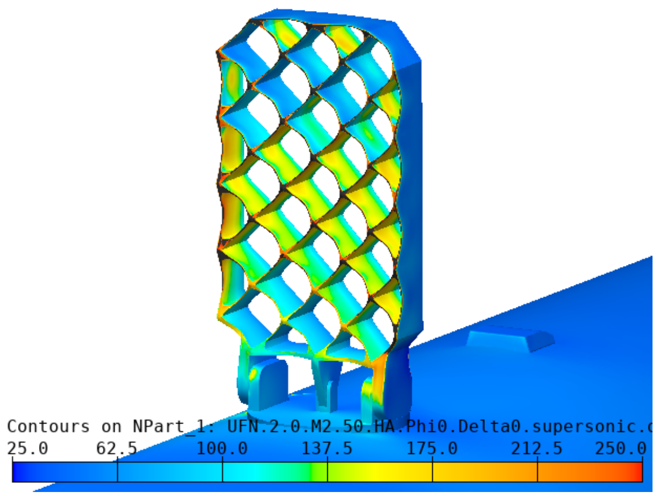

(b) new grid fin

Fig. 16. Pressure contours on the grid fin, $M_\infty = 2.50$, $\alpha = 180^o$.

Figure 16 shows the pressure contours on the old and new grid fin for a supersonic Mach number, and one can clearly observe the geometrical differences.

8. CONCLUSIONS

A large number of Navier Stokes simulations are being made for different configurations of the Themis T3 launcher to generate high-fidelity aerodynamic data bases that can be used in the development of the flight dynamics system. The calculation matrix and strategy were shortly summarized. Results for some configurations were discussed in detail.

9. REFERENCES

[1] E. Dumont et al, *CALLISTO - Reusable VTVL launcher first stage demonstratror*, 32nd ISTS, 2019.

[2] A. Marwege et al., “Retalt: review of technologies and overview of design changes,” *CEAS Space Journal*, vol. 14, 2022.

[3] A. Marwege, J. Klevanski, A. Gülhan, and J. Vos, *Building an Aerodynamic Model of a Vertical Landing Reusable Launcher based on CFD and Wind Tunnel Experiments in SALTO and CFD4SALTO*, 3rd FAR Conference, 2025.

[4] Y. Hoarau et al., *Recent Developments of the Navier Stokes Multi Block (NSMB) CFD solver*, AIAA Paper 6.2016-2056, 2016.

[5] J. Vos and D. Charbonnier, *CFD Simulations and Wind Tunnel Experiments for Re-usable Launch Vehicles*, 2nd FAR Conference, 2022.

[6] D. Charbonnier, J. Vos, A. Marwege, and C. Hantz, “Computational fluid dynamics investigations of aerodynamic control surfaces of a vertical landing configuration,” *CEAS Space Journal*, vol. 14, 2022.

[7] P. Spalart and S. Allmaras, *A one-equation turbulence model for aerodynamic flows*, AIAA Paper 6.1992-439, 1992.

[8] B.J. Mcbride, M.J. Zehe, and S. Gordon, *NASA Glenn Coefficients for Calculating Thermodynamic Properties of Individual Species*, NASA TP - 2002-211556, 2002.

[9] R.J. Kee et al., *A Fortran Computer Code Package for the Evaluation of Gas-Phase, Multicomponent Transport Properties*, SANDIA Report SAND86-8246, 1986.

[10] R.B. Bird et al., *Transport Phenomena, 2nd Edition*, John Wiley and Sons, New York, 2002.

[11] A. Jameson, W. Schmidt, and E. Turkel, *Numerical solutions of the Euler equations by finite volume methods using Runge-Kutta time stepping*, AIAA Paper 81.1259, 1981.

[12] S. Yoon and A. Jameson, *A Multigrid LU-SSOR Scheme for Approximate Newton Iteration Applied to the Euler Equations*, NASA-CR-179524, 1986.

[13] J. Neumann, *Parametric grid fin design study for the T3 vehicle within SALTO*, DGLR STAB Symposium, 2024.